Ghost hyperbolic surface polaritons in bulk anisotropic crystals

Weiliang Ma[1†], *Guangwei Hu*[2,3†], *Debo Hu*[4†], *Runkun Chen*[1†], *Tian Sun*[1], *Xinliang Zhang*[1*],
Qing Dai[4*], *Ying Zeng*[1], *Andrea Alù*[3,5*], *Cheng-Wei Qiu*[2*], *Peining Li*[1*]

1. Wuhan National Laboratory for Optoelectronics and School of Optical and Electronic Information, Huazhong University of Science and Technology, China
2. Department of Electrical and Computer Engineering, National University of Singapore, Singapore, Singapore
3. Photonics Initiative, Advanced Science Research Center, City University of New York, New York, NY, USA
4. CAS Key Laboratory of Nanophotonic Materials and Devices, CAS Key Laboratory of Standardization and Measurement for Nanotechnology, CAS Center for Excellence in Nanoscience, National Center for Nanoscience and Technology, Beijing 100190, China
5. Physics Program, Graduate Center, City University of New York, New York, NY, USA

[†] Equal contributions

[*] Correspondence to: xlzhang@hust.edu.cn; daiq@nanoctr.cn; aalu@gc.cuny.edu; chengwei.qiu@nus.edu.sg; lipn@hust.edu.cn

Polaritons in anisotropic materials have been enabling exotic optical features, of great interest for nanoscale light control. Here we report the first near-field observation of ghost phonon polaritons, propagating with in-plane hyperbolic dispersion on the surface of a polar uniaxial crystal, and at the same time exhibiting oblique wavefronts in the bulk. Ghost polaritons are a peculiar non-uniform surface wave solution of Maxwell's equations, arising at the surface of uniaxial materials whose optical axis is slanted with respect to the interface. They exhibit a peculiar bi-state nature, being both propagating, i.e., phase progressing, and evanescent, i.e., decaying, within the crystal, in contrast to conventional surface waves that are purely evanescent away from the interface. Our real-space near-field imaging experiments reveal long-distance (over 20 μm), ray-like propagation of deeply subwavelength ghost polaritons across the surface, verifying long-range, in-plane hyperlensing. At the same time, we show that the control of the out-of-plane angle of the optical axis enables hyperbolic-to-elliptic topological transitions at fixed frequency, providing an exciting route to drastically tailor the band diagram topology of surface polariton waves. Our results demonstrate a new phenomenon in polaritonics, offering opportunities to tailor nanoscale light in natural anisotropic crystals.

Natural crystals can exhibit extreme dielectric anisotropy, arising when the permittivity tensor elements along orthogonal optical axes have opposite signs. These features result in polaritons –light-matter hybrid electromagnetic excitations - with a hyperbolic dispersion, i.e., the polariton wavevector ***k*** can support hyperbolic iso-frequency contours (*1-3*). These hyperbolic polaritons have been first discovered in thin layers of van der Waals (vdW) crystals, such as hexagonal boron nitride (hBN) (*4-6*), alpha-phase molybdenum trioxide (α-MoO_3) (*7, 8*) and alpha-phase vanadium pentoxide (α-V_2O_5) (*9*). They feature nanoscale localization of the electromagnetic energy (*10, 11*), long polariton lifetimes (*12*), and enhanced photon density of states (*13*), facilitating various applications, such as sub-diffraction imaging (*14, 15*), thermal energy transfer (*16*), vibrational molecular sensing (*17, 18*), infrared light detection (*19*), and twisted nano-optics (*20-23*).

So far, two types of hyperbolic polaritons have been revealed: volume-confined hyperbolic polaritons (v-HPs) (*4, 5*) and surface-confined hyperbolic polaritons (*24, 25*) [s-HPs, also known as Dyakonov polaritons (*26*)]. V-HPs, propagating directionally inside low-loss crystals with a purely real-valued out-of-plane wavevector, have been mostly studied in the form of waveguide modes bounded within vdW thin films (*4*). In contrast, s-HPs, with a purely imaginary out-of-plane wavevector, are solutions of Maxwell's equations supported at the interface between two media, at least one of which should be anisotropic with its optical axis (OA) in the plane (*26*). They are characterized by a larger electromagnetic-field confinement, smaller group velocities, higher sensitivity to the environment, and similarly long lifetimes compared to v-HPs (*24*). S-HPs have been recently discovered at the edges of vdW flakes (*24, 25*), however no experiments have been able to directly image s-HPs on a sample surface. The challenge in observing s-HPs is in part associated with the fact that all previous studies on two-dimensional vdW materials have been restricted to scenarios in which their OA is either in-plane or out-of-plane, due to the challenge in post-processing its lattice orientation in thin films after being exfoliated from the bulk, posing inevitable limitations to the set of possible propagation features of the resulting polaritons.

Here we explore the scenario in which the OA of a bulk anisotropic crystal and its surface are not aligned, unveiling the existence of a fundamentally new type of anisotropic surface polaritons – ghost hyperbolic phonon polaritons (g-HPs). These light-matter hybrid quasiparticles arise from the coupling of infrared photons and lattice vibrations in anisotropic polar crystals with slanted OA, neither parallel nor perpendicular to the crystal surface. The g-HPs are the polaritonic analogue to the recently predicted ghost waves – a special type of non-uniform electromagnetic waves arising in anisotropic dielectric materials (*27, 28*). These waves, never experimentally observed, take their name from an analogy in their dispersion with ghost orbit bifurcation in the semiclassical theory of non-integrable quantum mechanical systems (*29*). Similarly, our g-HPs support a complex-valued out-of-plane wavevector within the crystal even in the absence of material loss. Thus, they are at the same time propagating (phase oscillating) and evanescent (exponentially decaying) inside the crystal. Over the crystal surface, they propagate with in-plane hyperbolic dispersion, enabling long-distance directional propagation of deeply subwavelength electromagnetic fields. Ghost phonon polaritons in layered metamaterials were predicted in a recent theoretical work (*30*), in which their in-plane hyperbolic dispersion had not been revealed.

To experimentally observe these phenomena, we use a calcite (calcium carbonate) crystal, widely exploited in optics for its tunable optical birefringence via OA alignment (*31, 32*). Its permittivity tensor can be written as $\varepsilon = diag\ [\varepsilon_\perp, \varepsilon_\parallel, \varepsilon_\perp]$, where $\varepsilon_\parallel$ and $\varepsilon_\perp$ are the principal components parallel and perpendicular to the OA, respectively. They have opposite signs in the mid-infrared Reststrahlen band from 1410 to 1550 cm^{-1}, $\varepsilon_\parallel > 0$ and $\varepsilon_\perp < 0$ (*33*), yielding strongly anisotropic phonon polaritons in calcite, which have surprisingly not been explored to the best of our knowledge. Owing to the formation of an oblique trigonal crystal structure, the OA in calcite typically forms a finite angle with respect to its surface (θ, defined as the angle between OA and interface, Fig. 1A). This feature provides a unique advantage for calcite, compared to other thin vdW layered nanomaterials, as the tilted angle θ can be nontrivially and finely tuned ($0^\circ < \theta < 90^\circ$) by mechanically cutting and polishing the sample, thus offering exquisite control of its overall polaritonic response (fig. S1) (*34*), and in particular the emergence of ghost hyperbolic surface polaritons.

To demonstrate the emergence of g-HPs due to an oblique OA, we solve the source-free Maxwell equations in the system of a dielectric background interfaced with the anisotropic calcite (Supplementary note S1). Assuming that the polariton wave in calcite, located at $z < 0$, carries a wavevector of (k_x, k_y, $-i{*}q_z$), its dispersion obeys

$$k_x^2 + k_y^2 - q_{z1}^2 = \varepsilon_\perp k_0^2 \qquad (1)$$

$$\frac{\left(k_y \cos\theta - i q_{z2} \sin\theta\right)^2}{\varepsilon_\perp} + \frac{k_x^2 + \left(k_y \sin\theta + i q_{z2} \cos\theta\right)^2}{\varepsilon_\parallel} = k_0^2 \qquad (2)$$

Here, q_{z1} and q_{z2} are associated with ordinary and extraordinary modes, respectively. To avoid unphysical divergence in the far field, the branch cut choice in the Riemann surface must ensure that the real part of q_z is positive. When $\theta = 0^\circ$, the OA is located within the interface, and the corresponding solutions yield s-HPs propagating along the surface with a purely real q_{z2} (*24, 25*); when $\theta = 90^\circ$, the OA is perpendicular to the interface, and surface-waves are not supported, since v-HPs have purely imaginary q_{z2} (*4,5*). Nontrivial values of θ ($0^\circ < \theta < 90^\circ$) induce solutions with a simultaneously nonzero real and imaginary value of q_{z2}, i.e., non-uniform waves, when $\varepsilon_\perp \cos^2\theta + \varepsilon_\parallel \sin^2\theta < 0$. This scenario corresponds to the emergence of g-HPs. More details are provided in supplementary note S1.

To study g-HPs arising at the calcite-air interface, we performed numerical simulations of dipole-excited polaritons on the (100) face of a semi-infinite calcite crystal (corresponding to $\theta = 23.3^\circ$, the dipole located at the height of 200 nm, Fig. 1A, see also supplementary note S2). The electric-field distribution above the surface shows concave wavefronts, a typical feature of in-plane hyperbolic polaritons (Fig. 1B, real part of E_z, $\omega = 1470\ \mathrm{cm}^{-1}$). The Fourier transform (FT) of the wavefronts reveals a hyperbolic isofrequency contour (IFC) in *k*-space (Fig. 1C), in excellent agreement with our analytical prediction based on source-free Maxwell equations (dashed lines in Fig. 1C, see supplementary note S1), unambiguously demonstrating the in-plane hyperbolic dispersion of calcite polaritons. We used a model solver to further visualize the polariton cross-sectional electric-field distribution (e.g., for the mode with an in-plane wavevector marked in Fig. 1C, see details in supplementary note S2). The electric-field map corroborates the existence of surface-bound propagation of calcite polaritons (Fig.1D), consistent with s-HPs (Fig. 1E) and distinct from v-HPs bounded within the layer (i.e., waveguide modes, such as the fundamental mode M0, Fig. 1F, see more details in fig. S2). Remarkably, the polaritons show oblique wavefronts inside the calcite bulk, with exponential attenuation but also sinusoidal phase oscillations, a highly unusual propagation feature, totally distinct from both s-HP and v-HP. This feature is associated with the complex wavevectors $q_{z,2}$ in our analytically derived polariton dispersion as shown in Fig. 1G and H. The oblique wavefronts strongly depend on the OA orientation and the direction of in-plane wavevectors (fig. S3), yielding a drastic reconfigurability of the polariton dispersion, as demonstrated below. These distinctive features show how g-HPs are a fundamentally new type of surface electromagnetic mode emerging in anisotropic crystals whose OA is not aligned with their surface.

For an experimental demonstration of subwavelength-scale confined g-HPs, we performed near-field imaging experiments aimed at visualizing in real space anisotropic polariton propagation along the surface (Fig. 2A). We fabricated a gold disk (diameter D =1.6 μm) on the (100) surface of a bulk calcite substrate ($\theta = 23.3^{\circ}$) (see supplementary note S3). The disk acts as an optical nanoantenna that concentrates p-polarized mid-infrared illumination (with an angle $\varphi = 30^{\circ}$ to the surface) into a local hot spot able to launch highly confined polaritons. The polariton field E_{p} propagates along the surface, interfering with the incident field E_{in}. The metallic tip of a scattering-type scanning near-field microscope (s-SNOM) records the interference field $E_{\mathrm{in}}+ E_{\mathrm{p}}$ when the sample is scanned (*6*), yielding the near-field optical image of polariton fields with nanoscale resolution (see supplementary note S4).

Figure 2B presents the near-field image of disk-launched polaritons measured at $\omega = 1460$ cm^{-1}. The polaritons exhibit concave wavefronts on the left of the disk, consistent with the numerical simulations in Fig. 1B. In striking contrast, on the right we measure ray-like (diffraction-less) polaritonic patterns extending for a distance of at least 20 μm (3 times the photon wavelength). Such long distance is remarkable, and it represents a record length for in-plane hyperbolic polaritons compared with previously observed values of around half of photon wavelength in natural materials (*7, 8*). The formation of polariton rays can be explained by stronger local fields (thus larger local photonic density of states) generated on the right portion of the disk owing to the oblique illumination (see further discussions in fig. S5). Our numerical simulations (with a plane wave source, incident angle $\varphi = 30^{\circ}$ consistent with the experiments) reproduce our experiments with an excellent agreement (fig. S6), confirming that the experimentally measured signals can be attributed to the disk and not a tip launching effect (noting that the simulations do not include the tip), as the polaritons launched by the tip are weakly reflected by the metal structure (*35*).

The FT of the near-field image in Fig. 2B shows two different hyperbolic IFCs in k-space (Fig. 2C), corresponding to the left and right parts of Fig. 2B, respectively mapped into the outer and inner IFCs (fig. S7). The difference between wavevectors (denoted as Δ) between the two IFCs stems from the asymmetric interference of the illuminating field and the polariton fields propagating on the antenna left and right sides (e.g., for k_x axis, the polariton propagating on the left side yielding $k_{x,\mathrm{left}} = k + \Delta/2$, the one propagating on the right side yielding $k_{x,\mathrm{right}} = k - \Delta/2$, $\Delta = 2k_0 \cos\varphi$) (*36*). The polariton in-plane wavevectors are also experimentally quantified,

$|k| > 5k_0$, larger than those of isotropic surface polaritons propagating over a single interface (*36*).

By altering the illumination frequency, we studied the frequency dependence of the anomalous ray-like propagation (Fig. 2D to G). Notably, the polariton ray's open angle α (definition in Fig. 2D) increases with the frequency, matching our numerical results (Fig. 2H). Indeed, all our experimental near-field images show an excellent agreement with numerical simulations (fig. S6), supporting the claim that we observe the g-HPs predicted in Fig.1.

The g-HPs feature long-distance ray-like propagation, as demonstrated in Fig. 2. Larger-wavevector, i.e., more confined, g-HPs can be launched by a smaller sized disk. This scenario is studied in Fig. 3A, in which we observe sharp polariton rays being launched on both sides of a small disk (D = 0.7 μm), in contrast to Fig. 2B. The more symmetric field distribution is explained by larger wavevector polariton fields (illustrated in Fig. 3C), which are much less influenced by the illuminating field, given by the wavevector mismatch (namely, $k >> \Delta$, thus $k_{x,\text{left}} \approx k_{x,\text{right}} \approx k$). The FT of Fig. 3A indeed corroborates the polariton large wavevectors, up to 23 k_0 (corresponding to a deeply subwavelength confinement $\lambda/23$, Fig. 3B and fig. S8). Notably, despite the increased wavevectors, the g-HP rays still travel for a significantly longer distance (> 15 μm) than v-HP rays observed in twisted vdW materials (~ 3 μm) (*20*-*23*).

The experimentally observed long-distance, highly confined, ray-like propagation of g-HPs suggests promising applications in deep subwavelength-scale information transfer. As an example, we demonstrate in-plane hyperlensing based on g-HPs in calcite – an effect that leverages ray-like polariton propagation to image subwavelength-scale objects. To this end, two gold disks were fabricated, and serve as the objects to be imaged (1.6-μm center-to-center separation) on the (100) surface of a calcite substrate (schematic in Fig. 3D). The recorded near-field image (Fig. 3E) corroborates the fact that the two disks, being excited by the external illumination, launch highly directional polaritonic rays propagating along the sample surface. Remarkably, these rays indeed transfer the subwavelength information of the objects (e.g., the ray's width strictly equals the disk diameter) to a distance larger than 15 μm. Importantly, several other applications requiring low-loss highly confined polaritons may benefit from our record-long propagation distance, including polaritonic networks, which may be further explored based on the results reported here.

Having established the exotic g-HPs and their enabling applications for hyperlensing, we discuss dispersion engineering of calcite ghost polaritons. Recently, it has been shown that the misalignment of OA in plane facilitates fine polariton dispersion control in twisted thin vdW materials (*20, 37*). Here, we demonstrate that the out-of-plane rotation of OA, resorting to easily tunable crystallographic orientation (angle θ) of calcite, can also manipulate the polariton propagation, without requiring any heterostructure, completing the OA-alignment induced polariton dispersion engineering in three dimensions. As illustrated in Fig. 4A, the angle θ can be effectively rotated by mechanically cutting the calcite crystal along different planes. For example, $\theta = 23.3^\circ$ is achieved via cutting along the plane (100), while $\theta = 90^\circ$ cuts along the plane (001). Varying the angle θ effectively rotates the bulk IFC of v-HPs in *k*-space (Fig. 4B, top panel), accordingly altering its projection on the k_x-k_y plane (bottom panels, grey areas in Fig. 4B), which may affect the condition $\varepsilon_\perp \cos^2\theta + \varepsilon_\parallel \sin^2\theta < 0$ necessary to support g-HPs. Note that the dispersion of g-HPs should be located outside the one of bulk IFCs, or equivalently, the whole k_x-k_y plane cannot be filled by the projected bulk IFC. Otherwise, for any possible in-plane momentum (k_x, k_y), the out-of-plane momentum is always real-valued, and the g-HPs with complex out-of-plane momentum cannot be supported (see supplementary note S1). As a result, the g-HPs, with their in-plane IFCs marked as blue dashed line in Fig. 4B, close to but different from the bulk IFC projection, can also be controlled by the angle θ.

For an experimental demonstration of crystallography-induced tunability of the g-HP dispersion, we show near-field images at $\omega = 1460$ cm^{-1} on three calcite samples with different OA orientations ($\theta = 23.3^o$, 48.5^o, and 90^o, respectively, Fig. 4C to E). The detailed sample information is shown in fig. S1. When $\theta = 23.3^o$ and $\theta = 48.5^o$, the polariton exhibits anisotropic (hyperbolic) in-plane propagation (Fig. 4, C and D; fig. S7 and S9). The polariton rays' open angle α increases with θ (Fig. 4F), in agreement with our theoretical model. On the other hand, we observe circular (isotropic) polariton propagation on the sample with $\theta = 90^o$ (Fig. 4E, fig. S10). This corresponds to a topological transition, with polaritons going from open hyperbolic to closed circular dispersions. As shown in Fig. 4G, varying θ yields a sign change of $\varepsilon_\perp \cos^2\theta + \varepsilon_\parallel \sin^2\theta$ from negative to positive, thus breaking the necessary condition for existence of g-HPs. Specifically, at $\omega = 1460$ cm^{-1} the g-HPs can only exist in the range below the critical angle (~ 57^o). For larger angles, v-HPs supporting waveguide modes are found on the surface (fig. S10). This tunability is robust and can also be found at other frequencies, as shown in supplementary fig. S11. Therefore, in combination with the recent observation of polariton topological transitions via in-plane OA alignment (*20, 37*), our demonstration of OA out-of-plane orientation in bulk calcite crystals shows how simple geometrical arguments can guide extreme dispersion engineering of polaritons supported in polar anisotropic materials.

Although we demonstrated g-HPs in calcite, these polaritons can emerge also in other natural anisotropic crystals, e.g., quartz (*38*). Our results also show that conventional bulk anisotropic crystals are exceptional candidates for exploring exotic polariton anisotropy, in addition to two-dimensional (2D) layered vdW materials that have recently drawn significant attention. They can be used as wafer-scale hyperbolic substrates for forming unique polaritonic heterostructures. Thanks to their three-dimensional nature, bulk anisotropic crystals provide a new dimension to support and control exotic polariton waves for applications in imaging, light guiding and information transfer at a deeply subwavelength scale.

References and Notes:

1. D. N. Basov, M. M. Fogler, F. J. García de Abajo, Polaritons in van der Waals materials. *Science* **354**, aag1992 (2016).
2. T. Low *et al.*, Polaritons in layered two-dimensional materials. *Nat. Materials* **16**, 182-194 (2017).
3. G. Hu, J. Shen, C.-W. Qiu, A. Alù, S. Dai, Phonon Polaritons and Hyperbolic Response in van der Waals Materials. *Adv. Opt. Mater.* **8**, 1901393 (2020).
4. S. Dai *et al.*, Tunable Phonon Polaritons in Atomically Thin van der Waals Crystals of Boron Nitride. *Science* **343**, 1125 (2014).
5. J. D. Caldwell *et al.*, Sub-diffractional volume-confined polaritons in the natural hyperbolic material hexagonal boron nitride. *Nat. Commun.* **5**, 5221 (2014).
6. P. Li *et al.*, Infrared hyperbolic metasurface based on nanostructured van der Waals materials. *Science* **359**, 892 (2018).
7. W. Ma *et al.*, In-plane anisotropic and ultra-low-loss polaritons in a natural van der Waals crystal. *Nature* **562**, 557-562 (2018).
8. Z. Zheng *et al.*, A mid-infrared biaxial hyperbolic van der Waals crystal. *Sci. Adv.* **5**, eaav8690 (2019).
9. J. Taboada-Gutiérrez *et al.*, Broad spectral tuning of ultra-low-loss polaritons in a van der Waals crystal by intercalation. *Nat. Materials* **19**, 964-968 (2020).
10. I.-H. Lee *et al.*, Image polaritons in boron nitride for extreme polariton confinement with low losses. *Nat. Commun.* **11**, 3649 (2020).
11. F. J. Alfaro-Mozaz *et al.*, Nanoimaging of resonating hyperbolic polaritons in linear boron nitride antennas. *Nat. Commun.* **8**, 15624 (2017).
12. A. J. Giles *et al.*, Ultralow-loss polaritons in isotopically pure boron nitride. *N Nat. Materials* **17**, 134-139 (2018).
13. P. Li *et al.*, Collective near-field coupling and nonlocal phenomena in infrared-phononic metasurfaces for nano-light canalization. *Nat. Commun.* **11**, 3663 (2020).
14. P. Li *et al.*, Hyperbolic phonon-polaritons in boron nitride for near-field optical imaging and focusing. *Nat. Commun.* **6**, 7507 (2015).
15. S. Dai *et al.*, Subdiffractional focusing and guiding of polaritonic rays in a natural hyperbolic material. *Nat. Commun.* **6**, 6963 (2015).
16. K.-J. Tielrooij *et al.*, Out-of-plane heat transfer in van der Waals stacks through electron–hyperbolic phonon coupling. *Nat. Nanotechnol.* **13**, 41-46 (2018).
17. M. Autore *et al.*, Boron nitride nanoresonators for phonon-enhanced molecular vibrational spectroscopy at the strong coupling limit. *Light: Sci. Appl.* **7**, 17172-17172 (2018).
18. A. Bylinkin *et al.*, Real-space observation of vibrational strong coupling between propagating phonon polaritons and organic molecules. *Nat. Photonics* **1**, 6 (2020).
19. S. Castilla *et al.*, Plasmonic antenna coupling to hyperbolic phonon-polaritons for sensitive and fast mid-infrared photodetection with graphene. *Nat. Commun.* **11**, 4872 (2020).

20. G. Hu *et al.*, Topological polaritons and photonic magic angles in twisted α-MoO_3 bilayers. *Nature* **582**, 209-213 (2020).
21. J. Duan *et al.*, Twisted Nano-Optics: Manipulating Light at the Nanoscale with Twisted Phonon Polaritonic Slabs. *Nano Lett.* **20**, 5323-5329 (2020).
22. Z. Zheng *et al.*, Phonon Polaritons in Twisted Double-Layers of Hyperbolic van der Waals Crystals. *Nano Letters* **20**, 5301-5308 (2020).
23. M. Chen *et al.*, Configurable phonon polaritons in twisted α-MoO_3. *Nat. Materials* **19**, 1307-1311 (2020).
24. P. Li *et al.*, Optical Nanoimaging of Hyperbolic Surface Polaritons at the Edges of van der Waals Materials. *Nano Lett.* **17**, 228-235 (2017).
25. S. Dai *et al.*, Manipulation and Steering of Hyperbolic Surface Polaritons in Hexagonal Boron Nitride. *Adv. Mater.* **30**, 1706358 (2018).
26. M. D'yakonov, New type of electromagnetic wave propagating at an interface. *Sov. Phys. JETP* **67**, 714-716 (1988).
27. E. N. Evgenii, Ghost resonance in anisotropic materials: negative refractive index and evanescent field enhancement in lossless media. *Adv. Photonics* **1**, 1-11 (2019).
28. W. I. Waseer, Q. A. Naqvi, M. J. Mughal, Non-uniform plane waves (ghost waves) in general anisotropic medium. *Opt. Commun.* **453**, 124334 (2019).
29. M. Kuś, F. Haake, D. Delande, Prebifurcation periodic ghost orbits in semiclassical quantization. *Phys. Rev. Lett.* **71**, 2167-2171 (1993).
30. Ghost surface phononic polaritons in ionic-crystal metamaterial. *J. Opt. Soc. Am. B* **35**, 2764-2769 (2018).
31. M. Ishigame, T. Satō, T. Sakurai, Splitting of the TO Mode in Calcite by the Polarization Field. *Phys. Rev. B* **3**, 4388-4391 (1971).
32. R. Frech, H. Nichols, Infrared reflectivity of calcite: Oblique phonons. *Physical Review B* **17**, 2775-2779 (1978).
33. K. H. Hellwege, W. Lesch, M. Plihal, G. Schaack, Zwei-Phononen-Absorptionsspektren und Dispersion der Schwingungszweige in Kristallen der Kalkspatstruktur. *Zeitschrift für Physik A Hadrons and nuclei* **232**, 61-86 (1970).
34. See supplementary materials.
35. E. Yoxall *et al.*, Direct observation of ultraslow hyperbolic polariton propagation with negative phase velocity. *Nat. Photonics* **9**, 674-678 (2015).
36. A. Huber, N. Ocelic, D. Kazantsev, R. Hillenbrand, Near-field imaging of mid-infrared surface phonon polariton propagation. *Appl. Phys. Lett.* **87**, 081103 (2005).
37. G. Hu, A. Krasnok, Y. Mazor, C.-W. Qiu, A. Alù, Moiré Hyperbolic Metasurfaces. *Nano Lett.* **20**, 3217-3224 (2020).
38. X. Wu, C. A. McEleney, M. González-Jiménez, R. Macêdo, Emergent asymmetries and enhancement in the absorption of natural hyperbolic crystals. *Optica* **6**, 1478-1483 (2019).

Competing interests:

The authors declare no competing financial interests.

Acknowledgements:

We thank the support from T.Wang for micro-FTIR measurements, Y.F.Hao and Y.S.Wang for antenna fabrication. P.L. acknowledges the support from the National Natural Science Foundation of China (Grant No. 62075070). C.-W.Q. acknowledges the support from the National Research Foundation, Prime Minister's Office, Singapore, under its Competitive Research Programme (CRP award NRF CRP22-2019-0006) and from the grant (R-261-518-004-720) from Advanced Research and Technology Innovation Centre (ARTIC). A.A. acknowledges the support from the Simons Foundation and the Department of Defense. Q.D. acknowledges the support from the National Natural Science Foundation of China (Grant No. 51925203). D.H. acknowledges the support from the National Natural Science Foundation of China (Grant No. 11704085). X.Z. acknowledges the support from the National Key Research and Development Program of China (Grant No. 2018YFA0704403).

Author contribution:

W.M., G.H., D.H., and R.C. contributed equally to this work. P.L. conceived the study. W.M. fabricated the samples. G.H. performed the theory analysis coordinated by C.Q., A.A. D.H. and W.M. performed the s-SNOM measurements with the help of T.S., Y.Z. G.H., R.C and W.M. performed the simulations. P.L., C.Q., A.A., Q.D., and X.Z. coordinated and supervised the work. W.M., G.H., A.A., C.Q., and P.L. wrote the manuscript with the input of all other co-authors.

Data and materials availability:

All data are available in the manuscript or the supplementary materials.

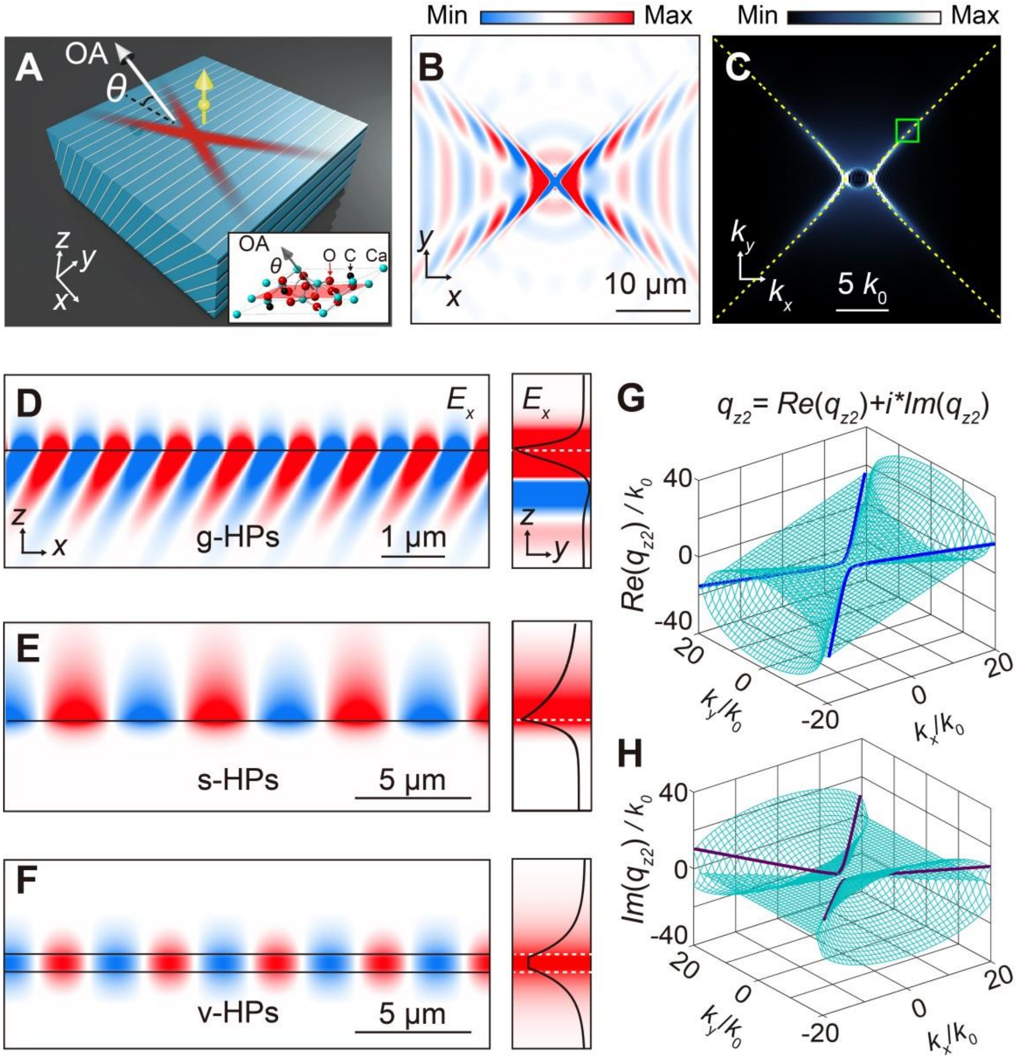

Fig. 1. Ghost hyperbolic surface phonon polaritons at the interface of bulk calcite crystal. (**A**) Schematic of a vertical dipole launching g-HPs at the interface of a bulk crystal of calcite. The OA is tilted at $\theta = 23.3^{\circ}$ to the surface. The inset illustrates the calcite crystal structure. (**B**) Simulated near-filed distribution Re(E_z) of dipole-launched polaritons above the surface at ω =1470 cm^{-1}. (**C**) Absolute value of the Fourier transform (FT) of the field distribution in panel (**B**). The dashed line shows the analytically calculated polariton dispersion. A green box denotes the g-HP mode with wavevector $|k|$= 7.1k_0, which is further analyzed in (**D**). (**D**) Left, cross-sectional near-field distribution of the g-HP mode [marked in panel (**C**)] propagating along the surface, Re(E_x). The solid black line denotes the air/calcite interface at z = 0. Right, corresponding g-HP profile in *y*-*z* plane. (**E**) Left, cross-sectional near-field distribution of a s-HP mode propagating along the surface, Re(E_x). Right, corresponding s-HP profile in *y*-*z* plane. (**F**) Left, cross-sectional near-field distribution of a v-HP waveguide mode (the fundamental M0 mode) along a thin layer, Re(E_x). Right, corresponding v-HP modal profile in the *y*-*z* plane. See more details of (D to E) in supplementary note S2. (**G**) and (**H**) Analytically calculated complex-valued q_{z2} of g-HPs in calcite: real part shown in (G) and imaginary part shown in (H). We note that the material loss is neglected in the simulations shown in Fig.1D-F, while adding the loss does not affect the results as shown in fig. S4.

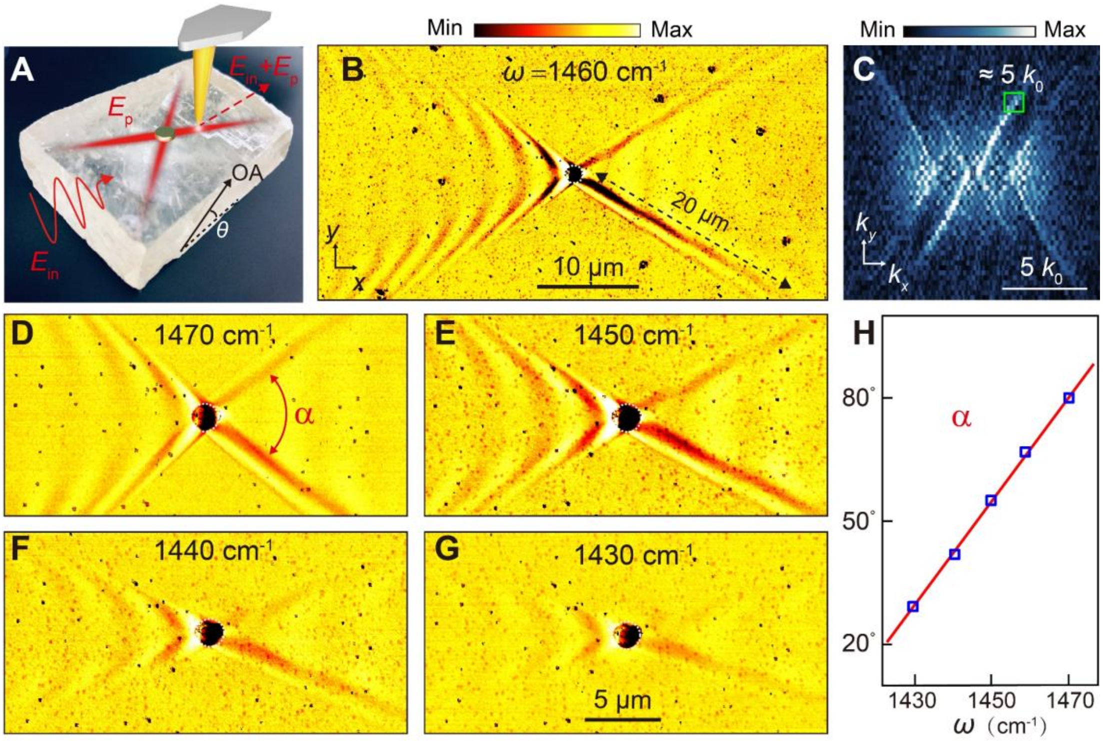

Fig.2. Real space imaging of antenna-launched g-HPs at the surface of bulk calcite. (**A**) Schematic of near-field imaging experiments (see sample information in fig. S1). (**B**) Experimental near-field image of antenna-launched g-HPs at the illuminating frequency $\omega = 1460\ \mathrm{cm}^{-1}$. The dashed line indicates the long travelling distance of the polariton rays (> 20 μm). The diameter of the disk antenna is D = 1.6 μm. (**C**) Absolute value of the FT of the image shown in the panel (**B**), scale bar is normalized to the photo wavevector k_0. The green spare indicates a component with wavevector $k = 5k_0$. (**D**) to (**G**) Near-field images recorded at four more illuminating frequencies. The red arrow in panel (**D**) indicates the open angle α of g-HPs rays (**H**) Frequency dependence of the open angle. Blue symbols are experimental data extracted from the images shown in (B), (D) to (G). The red line shows the simulation results.

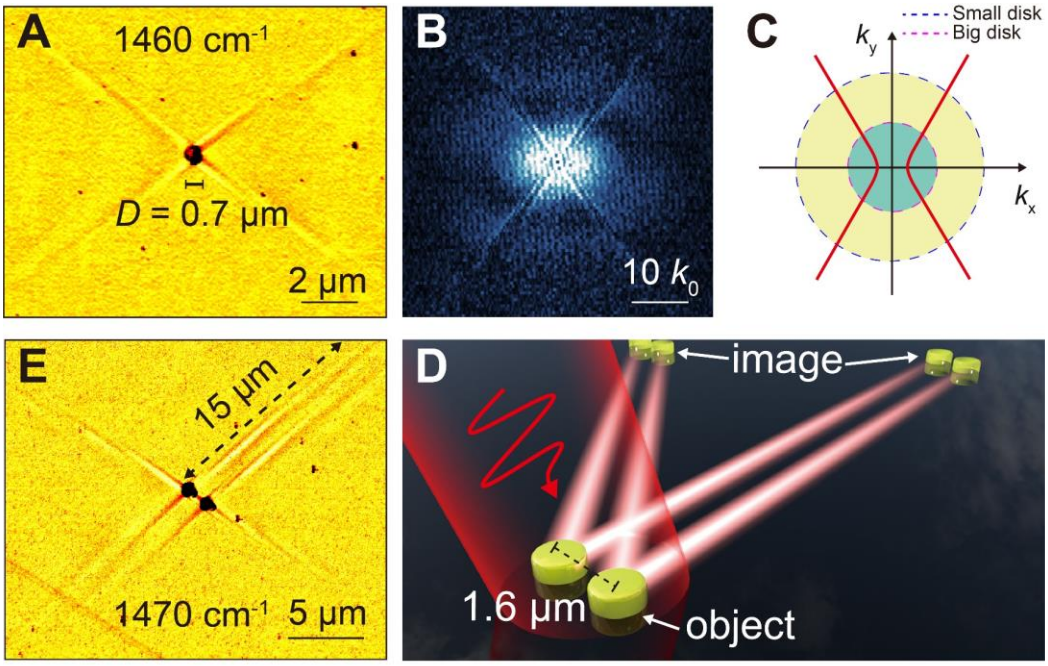

Fig. 3. Launching highly confined g-HPs for in-plane hyperlensing. (**A**) Near-field image of large wavevector g-HPs launched by a small antenna (diameter D = 0.7 μm), recorded at $\omega = 1460$ cm^{-1}. (**B**) Absolute value of the FT of the image shown in (A). (**C**) Sketch of the strategy of reducing the antenna's size for exciting large wavevector g-HPs. (**D**) Schematic illustration of the g-HP-based hyperlensing experiment. (**E**) Experimental verification of in-plane hyperlensing. The center-to-center distance between the two disks is 1.6 μm, and D = 0.65 μm. We note that the two disks, the illumination and the OA are not aligned, which thus causes the asymmetric field distribution.

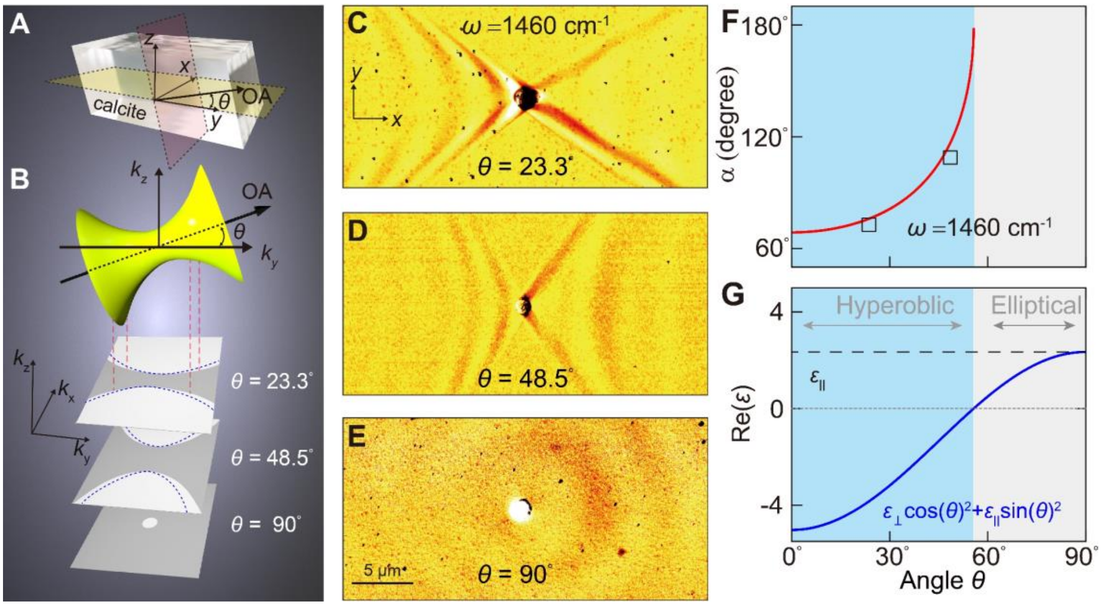

Fig. 4. Tunable hyperbolicity and topological transition of polaritons in calcite. (**A**) Schematic of selective plane in calcite. Its OA is within *y*-*z* plane, the interface between the calcite and background is within *x*-*y* plane, and the angle θ is defined between *y* axis and OA. Pale yellow surface corresponds to the characteristic plane (100) when θ = 23.3 °; while pale red surface is the characteristic plane (001) when θ = 90 °. (**B**) Schematic illustration of projected in-plane isofrequency contour, at θ = 23.3°, 48.5°, 90°. The 3D isofrequency surface (yellow surface) is projected to the k_x-k_y plane, with the grey regime denoting its shadow. When a mode with (k_x, k_y) locates within this shadow, the k_z should be real-valued, and mode therein is v-HPs. The g-HPs should only exist when a mode locates outside of its shadow and 0º<θ<90º, the schematic IFC of g-HPs are presented by blue dashed line. (**C**) – (**E**) Experimental near-field amplitude images at $\omega = 1460$ cm^{-1} with different tilted angle at $\theta = 23.3°$ (panel **C**), $\theta = 48.5°$ (panel **D**) and $\theta = 90°$ (panel **E**). (**F**) The experimentally measured open angle (α) of g-HPs (black square) vs the open angle of the shadow boundary of projected 3D isofrequency surface (red line). The g-HPs have a slightly smaller open angle. (**G**). The plots of the two projected effective in-plane permittivities ($\varepsilon_{\parallel}$ and $\varepsilon_{\perp}\cos^2\theta + \varepsilon_{\parallel}\sin^2\theta$) as a function of tilted angle θ at the frequency $\omega = 1460$ cm^{-1}. The hyperbolic regime (light blue) and elliptical regime (light gray) separate the case when the shadows of isofrequency surfaces partially or fully covers the k_x-k_y plane, respectively.

Supplementary Materials for

Ghost hyperbolic surface polaritons in bulk anisotropic crystals

Weiliang Ma[1†], *Guangwei Hu*[2,3†], *Debo Hu*[4†], *Runkun Chen*[1†], *Tian Sun*[1], *Xinliang Zhang*[1]*, *Qing Dai*[4]*, *Ying Zeng*[1], *Andrea Alù*[3,5]*, *Cheng-Wei Qiu*[2]*, *Peining Li*[1]*

1. Wuhan National Laboratory for Optoelectronics and School of Optical and Electronic Information, Huazhong University of Science and Technology, China
2. Department of Electrical and Computer Engineering, National University of Singapore, Singapore, Singapore
3. Photonics Initiative, Advanced Science Research Center, City University of New York, New York, NY, USA
4. CAS Key Laboratory of Nanophotonic Materials and Devices, CAS Key Laboratory of Standardization and Measurement for Nanotechnology, CAS Center for Excellence in Nanoscience, National Center for Nanoscience and Technology, Beijing 100190, China
5. Physics Program, Graduate Center, City University of New York, New York, NY, USA

[†] Equal contributions
[*]Correspondence to: xlzhang@hust.edu.cn; daiq@nanoctr.cn; aalu@gc.cuny.edu; chengwei.qiu@nus.edu.sg; lipn@hust.edu.cn

This PDF file includes:

Materials and Methods Notes. S1 to S4

Figs. S1 to S11

References (*1*-*8*)

Materials and Methods

Note S1. Theory to determine the g-HP propagation features

We solve source-free Maxwell equations to determine the dispersion of the g-HPs. The time convention is assumed $e^{-i\omega t}$. To do so, we first declare our geometry. Assume that the OA locates in global *y*-*z* plane, and the interface between isotropic background media (with permittivity ε_D) and anisotropic calcite locates at $z = 0$, where calcite locates at $z < 0$. The oblique angle (θ) of OA is defined between OA and *y* axis, where OA is along *y* axis when θ = 0 °and is along *z* axis when θ = 90 °.

With this definition, the permittivity of calcite in global Cartesian coordinates can be written as

$$[\bar{\bar{\varepsilon}}]_{xyz} = R_x(-\theta) \cdot diag[\varepsilon_\perp \quad \varepsilon_\parallel \quad \varepsilon_\perp] \cdot R_x(\theta) \quad \text{(S1)}$$

where $R_x(\theta)$ is the rotation matrix with respect to *x* axis. To solve the mode of surface waves associated with in-plane momentum (k_x, k_y) and for the simplicity of the eigenwave in each material, an auxiliary coordinate of $(\hat{\rho}, \hat{h}, \hat{z})$ is introduced and defined as

$$\hat{\rho} = \frac{1}{k_\rho}(k_x\hat{x} + k_y\hat{y}); \ \hat{h} = \hat{z} \times \hat{\rho} \quad \text{(S2)}$$

where $k_\rho = \sqrt{k_x^2 + k_y^2}$. Thus, the permittivity tensor of calcite in this auxiliary coordinates is written as

$$[\bar{\bar{\varepsilon}}]_{\rho hz} = R_z^{-1}(k_x, k_y) \cdot [\bar{\bar{\varepsilon}}]_{xyz} \cdot R_z(k_x, k_y) \quad \text{(S3)}$$

where $R_z(k_x, k_y)$ is the rotation matrix associated with transformation between global coordinate and auxiliary coordinate (*1*).

Assume that the mode in isotropic background has the out-of-plane momentum of iq_{z3} where

$$q_{z3} = \sqrt{k_\rho^2 - \varepsilon_D k_0^2} \quad \text{(S4)}$$

with both TE and TM wave component. ε_D is the permittivity of air. Here, $q_{z3} > 0$ to avoid the field divergence. The electric field of TE-mode is along $\hat{h}$ directions while the electric field of TM-mode has the basis of $\frac{1}{\varepsilon_D k_0}(iq_{z3}\hat{\rho} - k_\rho\hat{z})$.

Now, let's solve the mode in anisotropic calcite associated with the out-of-plane momentum of $-iq_z$, which is given by

$$\vec{k} \times \vec{k} \times \vec{E} + k_0^2\bar{\bar{\varepsilon}} \cdot \vec{E} = 0 \quad \text{(S5)}$$

with $\vec{k} = k_\rho \hat{\rho} - i q_z \hat{z}$. One can thus obtain the dispersion of the eigenwave inside calcite, which should have two solutions, i.e. ordinary (o-wave, with out-of-plane momentum q_{z1}) and extraordinary (e-wave, with out-of-plane momentum q_{z2}) component. For o-wave, it should

$$k_x^2 + k_y^2 - q_{z1}^2 = \varepsilon_\perp k_0^2 \quad \text{(S6)}$$

And for e-wave, it should follow

$$\frac{\left(k_y \cos\theta - i q_{z2} \sin\theta\right)^2}{\varepsilon_\perp} + \frac{k_x^2 + \left(k_y \sin\theta + i q_{z2} \cos\theta\right)^2}{\varepsilon_\parallel} = k_0^2 \quad \text{(S7)} \qquad .$$

This is also provided in main text. The eigenmode associated with each wave components $(E_\rho \hat{\rho} + E_h \hat{h} + E_z \hat{z})$ is given by Eq. S5, which should satisfy that

$$\gamma_{zj} = \frac{E_{z,j}}{E_{\rho,j}} = \frac{-\left(\varepsilon_{\rho z} k_0^2 - i q_{zj} k_\rho\right)\left(\varepsilon_{hh} k_0^2 - k_\rho^2 + q_{zj}^2\right) + \varepsilon_{\rho h} \varepsilon_{hz} k_0^2 k_0^2}{\left(\varepsilon_{zz} k_0^2 - k_\rho^2\right)\left(\varepsilon_{hh} k_0^2 - k_\rho^2 + q_{zj}^2\right) - \varepsilon_{hz} \varepsilon_{hz} k_0^2 k_0^2} \quad \text{(S8)}$$

$$\gamma_{hj} = \frac{E_{h,j}}{E_{\rho,j}} = \frac{-\left(\varepsilon_{\rho z} k_0^2 - i q_{zj} k_\rho\right) \varepsilon_{hz} k_0^2 + \varepsilon_{\rho h} k_0^2 \left(\varepsilon_{zz} k_0^2 - k_\rho^2\right)}{\left(\varepsilon_{hh} k_0^2 - k_\rho^2 + q_{zj}^2\right)\left(\varepsilon_{zz} k_0^2 - k_\rho^2\right) - \varepsilon_{hz} \varepsilon_{hz} k_0^2 k_0^2} \quad \text{(S9)}$$

where j is 1 for o-wave and 2 for e-wave.

With this, one can apply the boundary conditions that tangential E and H components are continuous, and find the dispersion of our reported g-HP waves. It is summarized below as

$$\frac{q_{z1} + q_{z3}}{q_{z2} + q_{z3}} = \frac{\gamma_{h2}}{\gamma_{h1}} \frac{\varepsilon_D k_0^2 + i q_{z3} k_\rho \gamma_{z1} - q_{z1} q_{z3}}{\varepsilon_D k_0^2 + i q_{z3} k_\rho \gamma_{z2} - q_{z2} q_{z3}} \quad \text{(S10)}$$

This is one major finding in this paper. Together with Eq. S4, Eq. S6-9, one could find the solutions of surface modes of g-HPs. It can be simply verified that, when $\theta = 0°$, this dispersion reduces to the conventional Dyakonov surface wave (*2*).

Out-of-plane momentum

For the frequency of interest in this paper between 1410 cm^{-1} and 1550 cm^{-1}, we have $\varepsilon_\parallel > 0$ and $\varepsilon_\perp < 0$. To avoid the unphysical divergence of field, we should choose that $\mathrm{Re}\left[q_{zj}\right] > 0$. Therefore, we can choose that $q_{z1} = \sqrt{k_\rho^2 - \varepsilon_\perp k_0^2}$. What is important is to find the solution of e-wave. According to Eq. S8, we can find that

$$q_{z2,\pm} = \frac{-i k_y (\varepsilon_\parallel - \varepsilon_\perp) \cos\theta \sin\theta \pm \sqrt{\Delta}}{\varepsilon_\parallel \sin^2\theta + \varepsilon_\perp \cos^2\theta}; \; \Delta = \varepsilon_\perp \left[k_y^2 \varepsilon_\parallel + (\varepsilon_\parallel \sin^2\theta + \varepsilon_\perp \cos^2\theta)(k_x^2 - k_0^2 \varepsilon_\parallel)\right] \quad \text{(S11)}$$

The general solution of q_{z2} should exist complex domain, which is plotted in Fig. 1G, H. Here, we discuss the solution in Eq. S11, with the remind that $\varepsilon_\parallel \sim 2.3 > 0$ and $\varepsilon_\perp < 0$.

- When $\varepsilon_{\parallel}\sin^2\theta + \varepsilon_{\perp}\cos^2\theta \geq 0$, i.e. $\theta \geq \alpha_0 \overset{\text{def}}{=} \operatorname{atan}\sqrt{-\frac{\varepsilon_{\perp}}{\varepsilon_{\parallel}}}$, we should have $\Delta < 0$ for sufficient large momentum. Thus q_{z2} is a purely imaginary number, that means that the mode (k_x, k_y) corresponds to a propagating wave inside the calcite. This is well-known volume-type hyperbolic polaritons.

  Note: Here, α_0 can be seen as the intrinsic open angle of the bulk isofrequency surface (IFS) of $\frac{k_{\perp}^2}{\varepsilon_{\parallel}} + \frac{k_{\parallel}^2}{\varepsilon_{\perp}} = k_0^2$, where $k_{\perp}^2 = k_{\perp 1}^2 + k_{\perp 2}^2$, with $k_{\perp 1}$ and $k_{\perp 2}$ being the momenta in two principle axis perpendicular to OA and $k_{\parallel}$ being the momentum parallel to OA (as shown in Fig. 4B of main text). The geometric condition $\theta > \alpha_0$ can be simply understood that for every possible mode of (k_x, k_y), we could find a solution of real k_z in this bulk IFS.

- When $\varepsilon_{\parallel}\sin^2\theta + \varepsilon_{\perp}\cos^2\theta < 0$, i.e. $\theta < \alpha_0$. In this case, we should be careful.
  - (i) Case i: $\Delta = 0$, i. e. $\frac{k_y^2}{\varepsilon_{\parallel}\sin^2\theta + \varepsilon_{\perp}\cos^2\theta} + \frac{k_x^2}{\varepsilon_{\parallel}} = k_0^2$, we have only purely imaginary q_{z2}, again reducing to a volume-type hyperbolic polaritons. Importantly, this condition is a hyperbolic line, which shows that we have degenerate solution of $q_{z2,+} = q_{z2,-}$. If one examines the shadow of bulk IFS projected to the plane of (k_x, k_y), this hyperbolic line corresponds to a boundary of the shadow as only for the momentum of (k_x, k_y) at this line gives a single value of q_{z2}.
  - (ii) Case ii: $\Delta < 0$, i. e. $\frac{k_y^2}{\varepsilon_{\parallel}\sin^2\theta + \varepsilon_{\perp}\cos^2\theta} + \frac{k_x^2}{\varepsilon_{\parallel}} < k_0^2$. This condition also only allows the purely imaginary value of q_{z2}, reducing a volume-type hyperbolic polaritons. In a geometry viewpoint, this condition says that the momentum of (k_x, k_y) locates within the shadow of bulk IFS projected to the plane of (k_x, k_y).
  - (iii) Case iii: $\Delta > 0$, i.e. $\frac{k_y^2}{\varepsilon_{\parallel}\sin^2\theta + \varepsilon_{\perp}\cos^2\theta} + \frac{k_x^2}{\varepsilon_{\parallel}} > k_0^2$.This condition gives that q_{z2} is a complex valued in general except that $\theta = 0°$ or 90°, which corresponds to dispersion of g-HPs and distinguishes from all previous types of polaritons. For $\theta = 0°$, this situation gives well-known Dyakonov surface wave; while for $\theta = 90°$, it reduces to a case of bulk uniaxial materials with OA perpendicular to interface.

Therefore, as a brief conclusion, we concluded two necessary conditions of existence of g-HPs are that $\varepsilon_{\parallel}\sin^2\theta + \varepsilon_{\perp}\cos^2\theta < 0$ and $\frac{k_y^2}{\varepsilon_{\parallel}\sin^2\theta + \varepsilon_{\perp}\cos^2\theta} + \frac{k_x^2}{\varepsilon_{\parallel}} > k_0^2$. A topological transition, from open to close dispersion line of polaritons with respect of in-plane dispersion of (k_x, k_y), can be induced by modifying the tilted angle of OA, thus breaking the first condition, as shown in fig. S10.

Note S2. Numerical simulations

Permittivity of the calcite crystal used in simulations

The uniaxial permittivity ($\varepsilon_{\text{calcite},\perp}$for the component in the direction perpendicular to the OA, $\varepsilon_{\text{calcite},\parallel}$ for parallel to the OA) of the calcite crystal was calculated by Lorentz oscillator models, where two Lorentz oscillators were used for $\varepsilon_\perp$ and one oscillator for $\varepsilon_\parallel$ according to

$$\varepsilon_\perp = \varepsilon_{\infty,1}\left(1+\frac{\omega_{\text{LO},1}^2-\omega_{\text{TO},1}^2}{\omega_{\text{TO},1}^2-\omega^2-i\omega\Gamma_1}+\frac{\omega_{\text{LO},2}^2-\omega_{\text{TO},2}^2}{\omega_{\text{TO},2}^2-\omega^2-i\omega\Gamma_2}\right) \quad (\text{S12})$$

$$\varepsilon_\parallel = \varepsilon_{\infty,3}\left(1+\frac{\omega_{\text{LO},3}^2-\omega_{\text{TO},3}^2}{\omega_{\text{TO},3}^2-\omega^2-i\omega\Gamma_3}\right) \quad (\text{S13})$$

ω_{TO} and ω_{LO} are the TO and LO phonon frequencies, respectively. Γ is the damping constant. ε_∞ is the high-frequency permittivity. For $\varepsilon_\perp$, we took $\varepsilon_{\infty,1}$= 2.7, $\omega_{\text{TO},1}$ = 712 cm^{-1}; $\omega_{\text{LO},1}$ = 715 cm^{-1}; Γ_1= 5 cm^{-1}. $\omega_{\text{TO},2}$ = 1410 cm^{-1}; $\omega_{\text{LO},2}$ = 1550 cm^{-1}; Γ_2= 10 cm^{-1}. For $\varepsilon_\parallel$, we took $\varepsilon_{\infty,3}$= 2.4, $\omega_{\text{TO},3}$ = 871 cm^{-1}; $\omega_{\text{LO},3}$ = 890 cm^{-1}; Γ_3= 3 cm^{-1} the parameters above are from reference (*3*). For best matching of our simulated and experimental results (see supplementary fig. S6), we slightly changed the value in reference (*3*) and used Γ_1= 5 cm^{-1}; $\omega_{\text{TO},2}$ = 1410 cm^{-1}, $\omega_{\text{LO},2}$ = 1550 cm^{-1}; $\omega_{\text{TO},3}$ = 871 cm^{-1}, Γ_3= 3 cm^{-1}.

General simulations information

We used a finite-element numerical simulation software (COMSOL) to simulate near-field distributions of polaritons propagating along the calcite's surface. The mode solver module of COMSOL was used for the quasi-normal mode analysis of g-HPs.

Simulations details for Figure 1.

For the simulation shown in Fig. 1B, an electric dipole source was used to excite polaritons in calcite. The uniaxial permittivity used for simulation is $\varepsilon_\parallel$ = 2.34, $\varepsilon_\perp$ = -3.74+0.55i (the solutions to Equation S12 and S13 at ω = 1470 cm^{-1}, supplementary Note S2). The calcite OA lays with an angle of θ= 23.3 ° to the (100) surface. The dipole source is located at 200 nm above the calcite's surface. The near-field distribution was taken from the plane at 50 nm above the calcite's surface. The Fourier transform (FT) shown in Fig. 1C was obtained with the software Gwyddion. The theoretical IFC curve was analytically calculated by following the processes shown in supplementary Note S1.

For the mode analysis of the g-HP mode shown in Fig. 1D, we considered calcite as a semi-infinite uniaxial crystal with lossless permittivity $\varepsilon_{\|} = 2.34$, $\varepsilon_{\perp} = -3.74$ at $\omega = 1470$ cm^{-1}. The calcite's OA aligns with the angle of $\theta = 23.3°$ to the top surface. We used two-dimensional (2D) mode solver of COMSOL to calculate the modal profile of the g-HP mode with the wave vector $k = 7.1k_0$ (indicated by a green symbol on the FT results shown in Fig. 1C of the main text). The obtained modal profile is shown in the right panel of Fig. 1D. By combing two COMSOL modules, the boundary mode analysis and the frequency-domain study, we calculated the polariton mode's electric field distribution E_x along the propagation direction (cross section in the x-z plane). The results are shown in the left panel of Fig. 1D.

For the s-HP mode shown in Fig. 1E, we considered a semi-infinite uniaxial crystal with the lossless permittivity $\varepsilon_{\|} = 2.34$, $\varepsilon_{\perp} = -3.74$ (the same as that in Fig. 1D) but with the OA aligning in the direction parallel to the surface. In this case, s-HPs can exist at the top surface of the crystal, which has been studied at the edges of thin flakes of hBN (*4*, *5*). By following the same methods used in Fig. 1D, we calculated the modal profiles of the s-HP mode with the wave vector $k = 1.17k_0$ and show the results in Fig. 1E.

For the v-HP mode shown in Fig. 1F, we considered a 500 nm-thick layer of a uniaxial crystal with lossless permittivity $\varepsilon_{\|} = 2.34$, $\varepsilon_{\perp} = -3.74$ (the same as that in Fig. 1D and E) but the OA is perpendicular to the surface. In this case, v-HPs are confined between two interfaces, forming the different-ordered waveguide modes propagating along the layer (*6*). By following the same methods used in Fig. 1D, we calculated the modal profiles of the s-HP modes. The results of the fundamental waveguide mode M0 with the wave vector $k = 1.53k_0$ are shown in Fig. 1F of the main text. The results of higher order modes, M1 and M2, are shown in supplementary fig. S2.

<u>Simulations details for Figure 2.</u>

For obtaining the frequency dependence of the g-HP ray's open angle α shown in Fig. 2H, we simulated the near-field distribution of disk-launched g-HPs at different frequencies (see supplementary fig. S6). In the simulations, the disk was illuminated by a *p*-polarized plane wave with incident angle of 30° relative to surface. All near-field distributions were recorded at a height of 50 nm above the calcite surface.

Note S3. Materials and fabrication

We used large-sized calcite substrates (size: 1cm×1cm; 1-mm-thick; different OA-orientation angles; see supplementary fig. S1) commercially available from Hefei Kejing in China, which were prepared by mechanical cleavage from bulk calcite single crystals (trigonal structures). Atomic force microscope (AFM) characterized the nanoscale smoothness of all the calcite substrates. Gold disk antennas were fabricated on the calcite surface via standard electron beam lithography. The disk patterns were written on the resist (PMMA: 495/A4, thickness ≈ 100 nm) spin-coated on the calcite substrate. The standard lift-off procedure was used after the e-beam evaporation of Ti (3 nm)/Au (40 nm) onto the developed resist.

Note S4. Near-field microscopy

For near-field imaging experiments, we used a s-SNOM system commercial from Neaspec GmbH based on an atomic force microscope (AFM). The Pt-coated AFM tip oscillates vertically with an amplitude of about 50 nm at a frequency $\Omega \approx 270$ kHz. It is illuminated by light from a wavelength-tunable continuous-wave quantum cascade laser (range from 1310 to 1470 cm^{-1}). The backscattered light is collected with a pseudo-heterodyne interferometer (*7*). To suppress background contribution in the tip-scattered field, the interferometric detector signal is demodulated at a higher harmonic $n\Omega$ ($n \geq 2$), yielding near-field amplitude s_n and phase φ_n images. Figs. 2-4 show amplitude s_2 images.

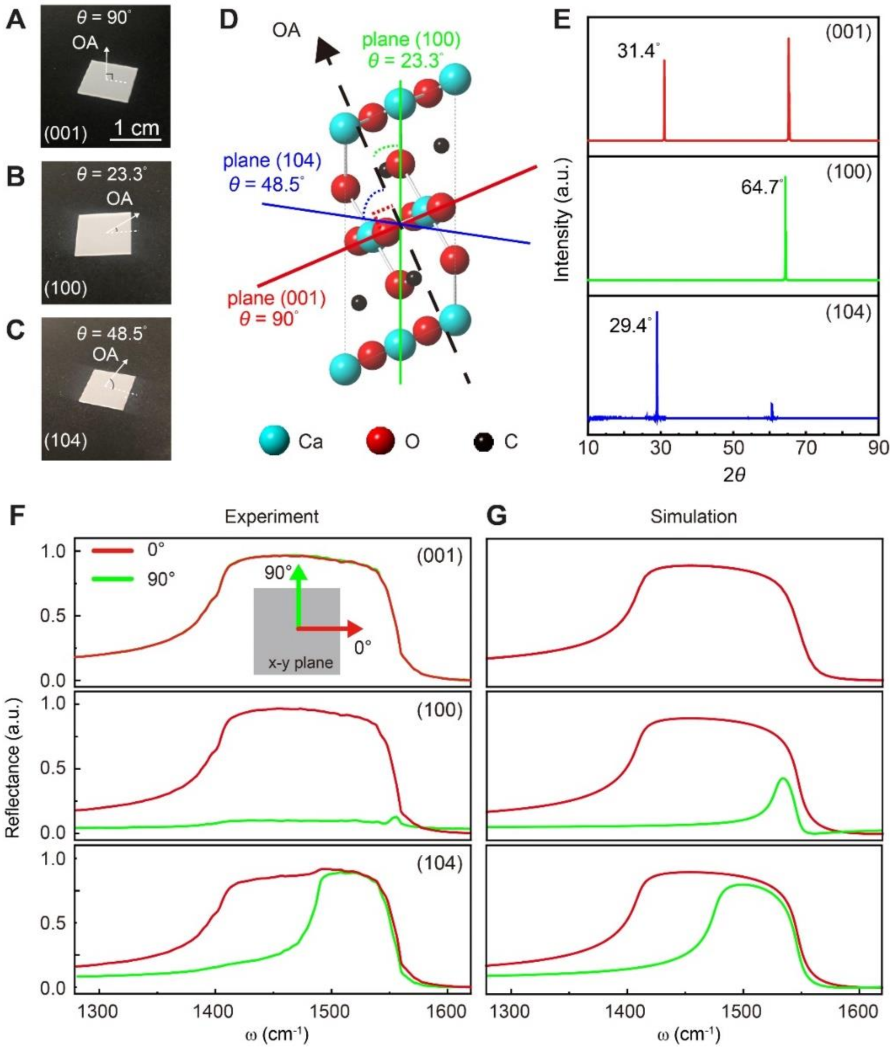

Figure S1. Centimeter-sized calcite substrates with different OA-orientations and corresponding XRD patterns, angle-resolved far-field reflectance. (**A** to **C**) Optical microscope images of calcite substrates for θ = 90°, 23.3°, 48.5° [the crystal surface is along plane (001), (100), (104), respectively]. (**D**) Schematics of the characteristic planes and the corresponding angle θ with respect to OA. Black dashed arrow represents OA. Green, red and blue lines indicate the characteristic plane (100), (001), (104), respectively. (**E**) X-ray diffraction (XRD) data of calcite substrates with different angles with respect to OA. XRD patterns of three calcite substrates with different θ exhibited strong diffraction peaks at 31.4°, 64.7°, 29.4° indicating the characteristic plane (001), (100) and (104) of calcite, respectively. (**F**) FTIR reflection spectra of calcite substrates shown in (**A** to **C**) for different polarization angles of the incident light. The 0° polarization defined here is parallel with direction of red arrow in x-y plane. (**G**) Theoretically fitted spectra using the dielectric permittivities according to supplementary Note S2. The results for the calcite substrates for θ = 90° [the surface is along plane (001)], θ = 23.3° [the surface is along plane (100)] and θ = 48.5° [the surface is along plane (104)], respectively.

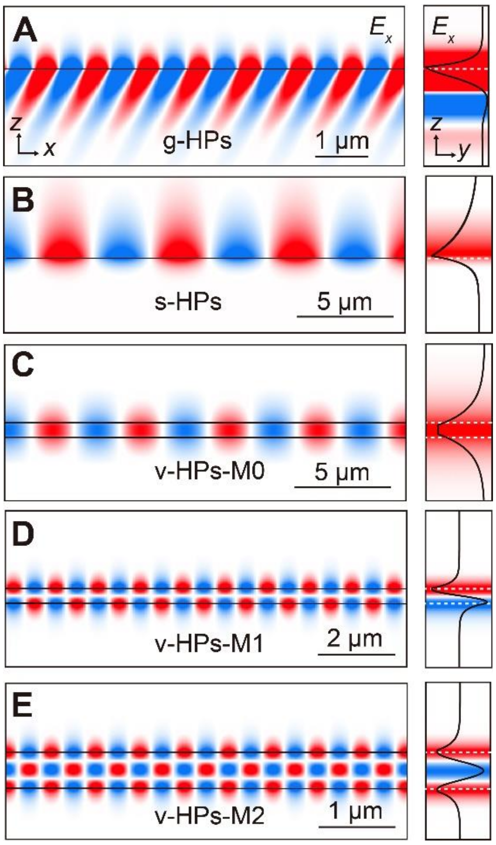

Figure S2. Comparison of the modal patterns of the g-HPs, s-HPs and v-HPs. (A to C) Transverse cross-section of the simulated near-field distributions of a g-HPs mode, s-HPs mode, and the fundamental v-HPs waveguide mode M0, respectively. These results are shown in Fig. 1 of main text. (**D** and **E**) Near-field distributions of the higher order v-HPs waveguide modes, M1 and M2, respectively. The s-HPs possess pure imaginary-valued k_z and thus exponentially decay inside the crystal. The v-HPs exhibiting real-valued wave vector k_z in the material. They thus can accumulate the phase variations in the vertical direction to form Fabry–Pérot interferences between the two interfaces, resulting the different order waveguide modes. In contrast, as a consequence of the oblique wavefronts, the g-HPs exhibit an unusual propagation feature - their electric fields exponentially attenuate with sinusoidal phase oscillations inside calcite.

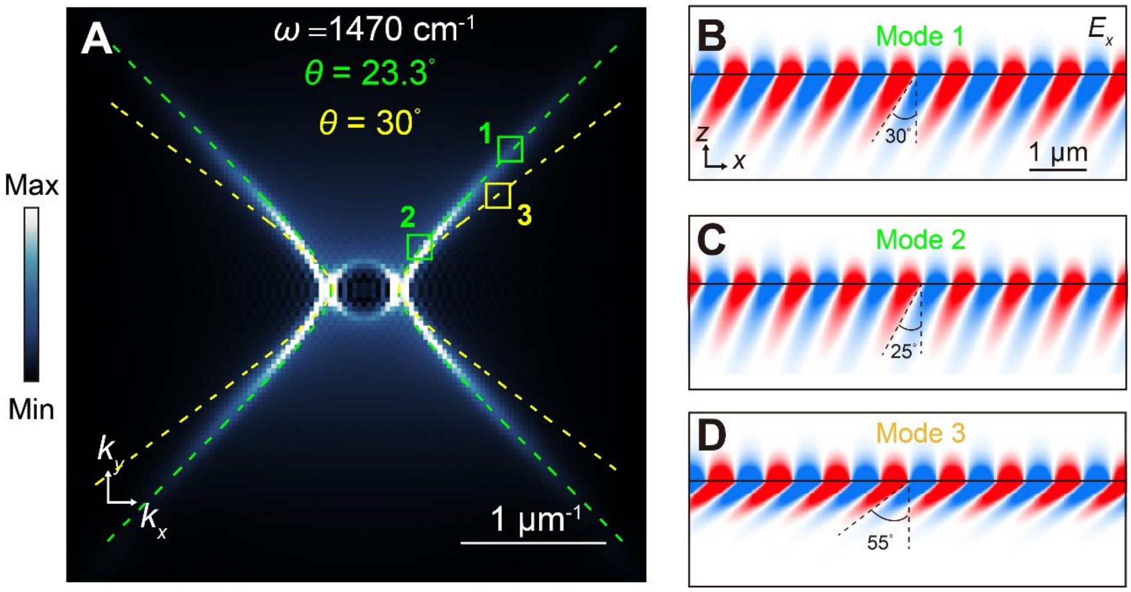

Figure S3. Oblique polariton wavefronts in calcite depending on the angle θ and in-plane wave vector. (**A**) False-color map, FT results (for the calcite crystal OA orientated with $\theta = 23.3°$) shown in Fig.1C of main text. Dashed green line, corresponding theoretical IFC of in-plane wave vectors. Dashed yellow line, the theoretical IFC for the OA orientation with $\theta = 30°$. (**B** to **D**) Near-field distribution of three distinct g-HP modes, which are marked by green and yellow symbols in (A), respectively. It is clear that the oblique angle of the g-HP modes within calcite varies with the change of the angle θ and in-plane wave vector.

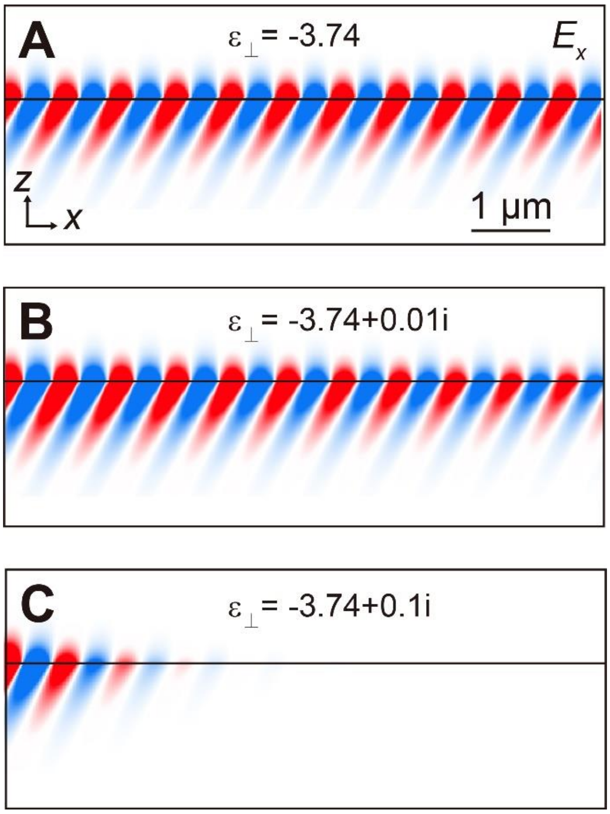

Figure S4. Numerical simulations of g-HPs considering the material loss. (**A** to **C**) Transverse cross-section of the simulated near-field distribution of a g-HP mode for different losses. It is clear that the g-HPs still exist in the existence of the loss. However, the propagation length is reduced when adding the loss. For all the cases we use the $\varepsilon_{\|} = 2.34$.

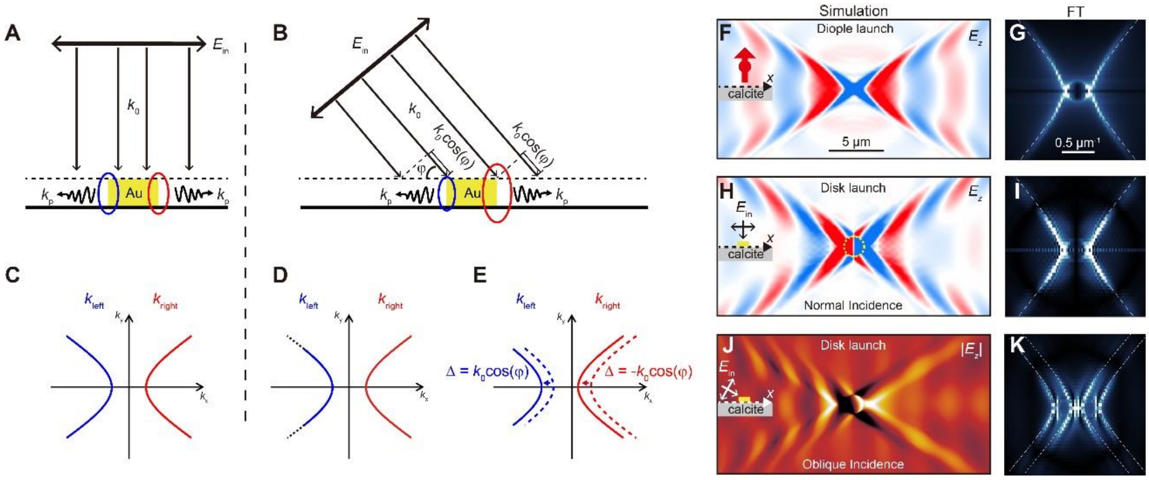

Figure S5. Explanation for the observed asymmetric field distribution of disk-launched g-HPs. (**A**) Schematic, symmetric excitation of the disk antenna by normal-incident illumination for exciting the polaritons. The blue and red ellipses illustrate the near-field “hot spots” generated at the left and right ends of the disk antenna, yielding the symmetrical distribution of g-HP wave vectors as indicated in (**C**). (**B**) Schematic, asymmetric excitation of the disk antenna by oblique-incident illumination, yielding the asymmetrical near-field “hot spots” at the disk’s two extremities: the near-fields at the disk’s left extremity are stronger than that at the antenna’s right side. As a result, the polaritons exhibit asymmetric distribution of wave vectors as sketched in (**D**). The disk right extremity excites more g-HP modes (indicated by a longer IFC curve) forming the polariton ray patterns, as compared to the polaritons on the left side exhibiting the patterns of polariton wavefronts. Furthermore, the excited polaritons propagate away from the disk, interfering with the illuminating field. Owing to the oblique illumination, the spacing distance of interference fringes is given by $\delta_l = 2\pi/(k_p+k_0 \cos\varphi)$ for the disk’s left side and $\delta_r = 2\pi/(k_p-k_0\cos\varphi)$ for the right side, respectively (*8*). Thus, the IFCs of wave vectors illustrated in (**E**) are shifted by $\pm\ k_0\cos\varphi$. (**F**) Simulated near-field distribution E_z of dipole-launched g-HPs on calcite ($\theta = 23.3°$) at $\omega = 1460\ \text{cm}^{-1}$. (**G**) FT of the image shown in (F). The white dashed line is the theoretical IFC. (**H**) Simulated near-field distribution of g-HPs launched by the disk antenna (diameter D =1.6 μm) on calcite with normal-incident illumination, corroborating the symmetric distribution of polariton fields. (**I**) FT of the image shown in (H), revealing the IFC of polariton wave vectors fitting very well with the theoretical results (dashed white line). (**J**) Simulated near-field distribution of g-HPs launched by the disk antenna on calcite with oblique-incident illumination ($\varphi = 30°$), exhibiting the asymmetric polariton field distribution. (**K**) FT of the image shown in (**J**), revealing two sets of IFC of polariton wave vectors. The outer one corresponds to the polaritons propagating on the disk’s left side. The inner one corresponds to the polaritons propagating on the disk’s right side. These two IFCs fit very well with two theoretical results obtained by shifting the theoretical IFC (i.e., dashed line shown in G) with $\pm\ k_0\cos\varphi$, respectively, according to the analysis shown in (D and E).

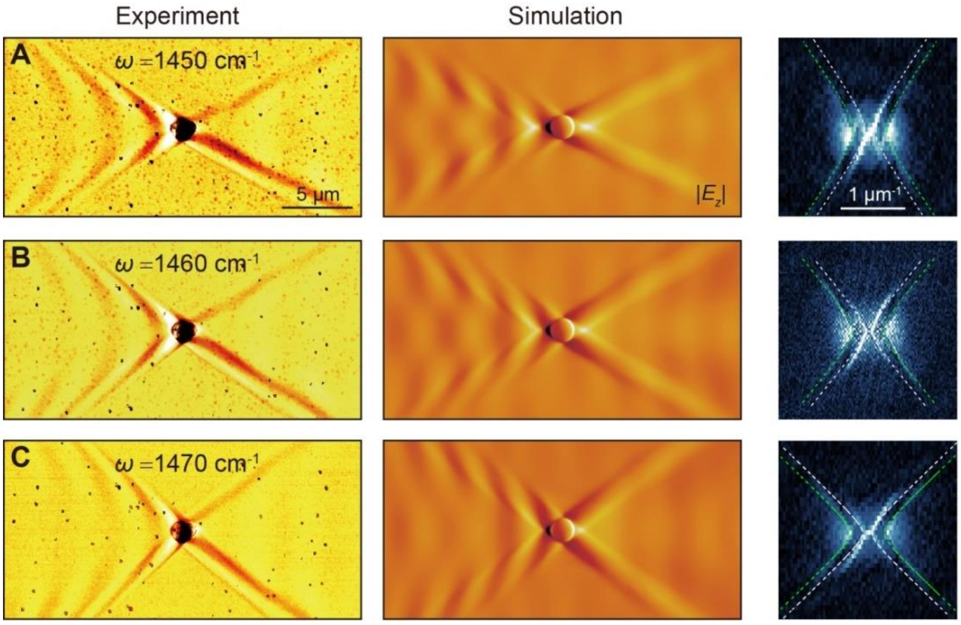

Figure S6. Comparison of experimental and simulated near-field images of disk-launched g-HPs. (**A** to **C**) Disk-launched g-HPs at three different frequencies: ω = 1450 cm^{-1}, ω = 1460 cm^{-1}, and ω = 1470 cm^{-1}, respectively. Left: Experimental near-field images of g-HPs. Middle: Simulated near-field images of disk-launched g-HPs. Left: FT of the experimental near-field images shown in left panel. Green and white lines are theoretical IFCs of in-plane wave vectors by considering the interference factors ($\pm\ k_0\cos\varphi$) according to supplementary fig. S5. Considering that the metallic s-SNOM tip is not included in the calculations, we thus assign the experimental near-field distribution to disk-launched polaritons.

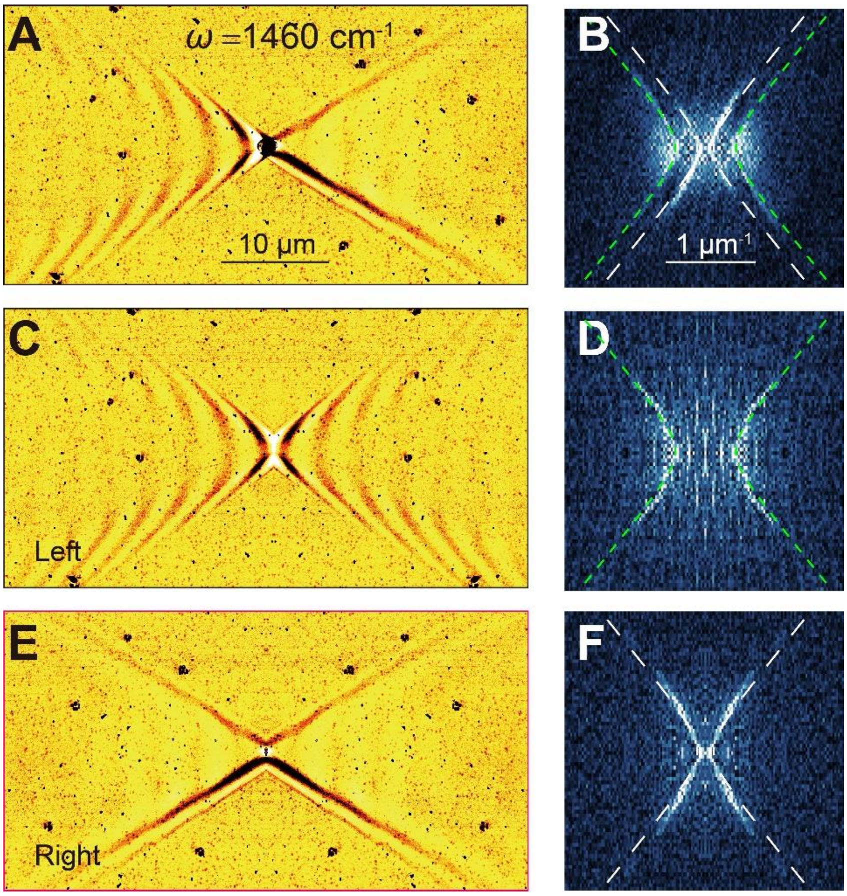

Figure S7. Analysis of experimental near-field images of disk-launched g-HPs on calcite (θ = 23.3 °). (**A**) Experimental near-field image of disk-launched g-HPs on calcite at ω = 1460 cm^{-1}, shown in Fig. 2B of the main text. (**B**) FT of the image in panel (A), revealing two hyperbolic IFCs of in-plane wave vectors. These experimental IFCs fit very well with the theoretical results (green and white lines, considering the interference factors ($\pm k_0 \cos\varphi$), respectively, according to supplementary fig. S5) (**C**) Synthetic image obtained by merging original and horizontally flipped images of the left part of panel (A). This procedure isolates the polaritons propagating in the left part of the disk antenna, and also increases the number of image pixels for the subsequent FT analysis, in order to increase the number of pixels in the FT process and thus its quality. (**D**) FT of the synthetic image shown in panel (C), revealing a hyperbolic IFC matching the theoretical IFC (green line) with large wave vectors shown in panel (B). (**E**) Synthetic image obtained by merging original and horizontally flipped images of the right part of the image shown in panel (A). (**F**) FT of the image shown in panel (E), revealing a hyperbolic IFC matching the theoretical IFC (white line) with small wave vectors shown in panel (B). To conclude, the two hyperbolic IFCs observed in (B) correspond to the polariton-wave patterns observed in the left and right parts of the image (A), respectively, arising from the asymmetric excitation of the disk antenna and asymmetric interference of the illuminating field according to supplementary fig. S5. From the FT analysis, we also conclude that the image shown in panel (A) does not contain the tip-excited, disk-edge-reflected polaritons that should exist in both side of the image as they are independent on the illumination direction.

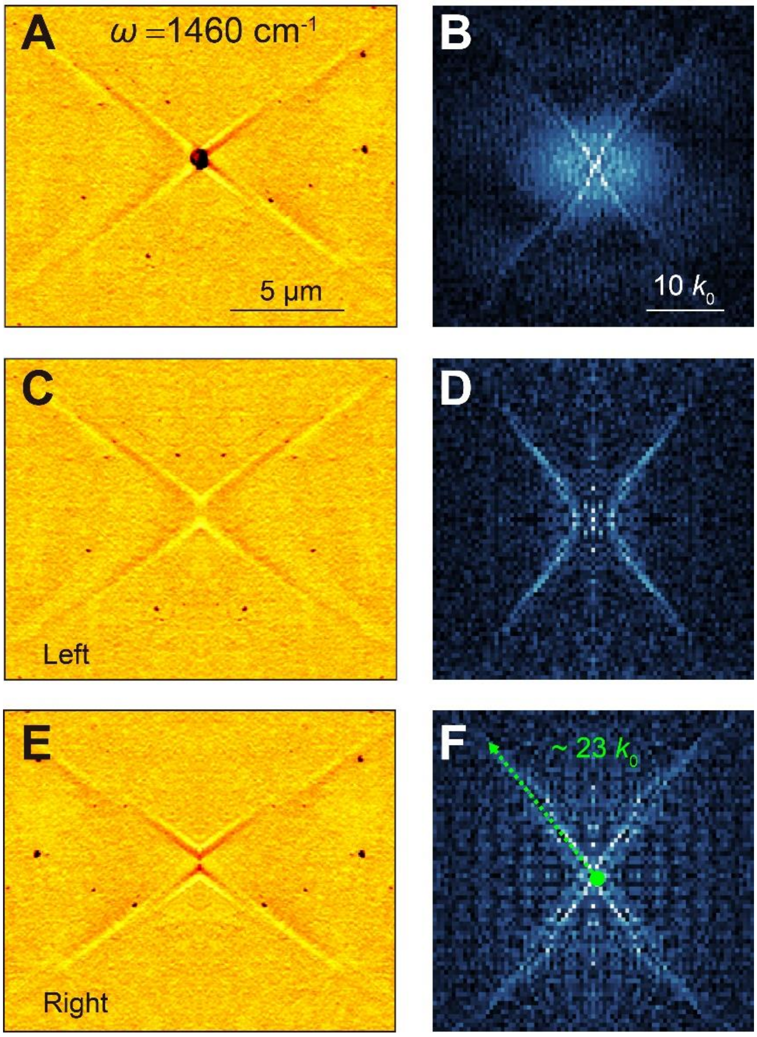

Figure S8. Analysis of experimental near-field images of g-HPs (launched by small-sized disk) on calcite ($\theta = 23.3°$). (**A**) Experimental near-field image of g-HPs (launched by small-sized disk, D = 0.7 μm) on calcite at ω = 1460 cm^{-1}, shown in Fig. 3A of the main text. (**B**) FT of the image in panel (A), revealing two hyperbolic IFCs of in-plane wave vectors. (**C**) Synthetic image obtained by merging original and horizontally flipped images of the left part of panel (A). (**D**) FT of the synthetic image shown in panel (C), revealing a hyperbolic IFC. (**E**) Synthetic image obtained by merging original and horizontally flipped images of the right part of the image shown in panel (A). (**F**) FT of the image shown in panel (E), revealing a hyperbolic IFC. The green arrow indicates a g-HPs mode with wavevector $k = 23\ k_0$ which is larger than the mode launched by large disk shown in Fig. 2.

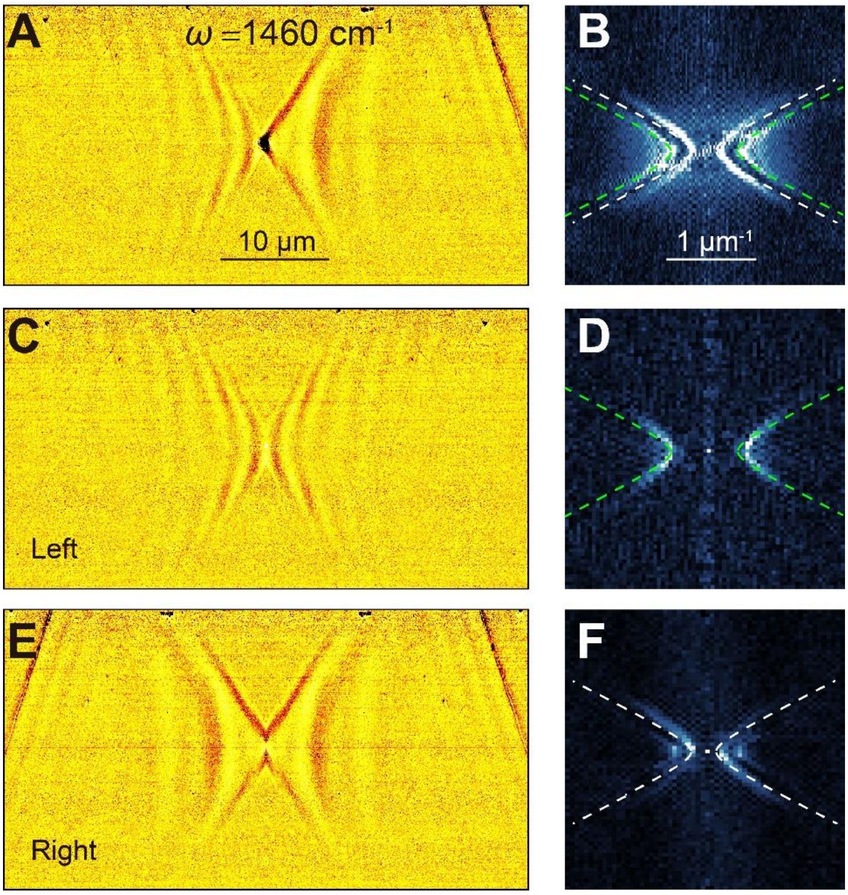

Figure S9. Analysis of experimental near-field images of disk-launched g-HPs on calcite (θ = 48.5 °). (**A**) Experimental near-field image of disk-launched g-HPs on calcite at ω = 1460 cm^{-1}, shown in Fig. 4D of the main text. (**B**) FT of the image in panel (A), revealing two hyperbolic IFCs of in-plane wave vectors. These experimental IFCs fit well with the theoretical results (green and white lines, considering the interference factors $\pm k_0\cos\varphi$, respectively, according to supplementary fig. S5) (**C**) Synthetic image obtained by merging original and horizontally flipped images of the left part of panel (A). This procedure isolates the polaritons propagating in the left part of the disk antenna, and also increases the number of image pixels for the subsequent FT analysis, in order to increase the number of pixels in the FT process and thus its quality. (**D**) FT of the synthetic image shown in panel (C), revealing a hyperbolic IFC matching the theoretical IFC (green line) with large wave vectors shown in panel (B). (**E**) Synthetic image obtained by merging original and horizontally flipped images of the right part of the image shown in panel (A). (**F**) FT of the image shown in panel (E), revealing a hyperbolic IFC matching the theoretical IFC (white line) with small wave vectors shown in panel (B). The FT in panel (F) also reveals weak hyperbolic features at larger wave vectors, which do not appear in the FT in panel (D). We do not think these weak features arise from the tip-excited, Au-disk-reflected polaritons that should exist in both side of the disk antenna. Their origin could be explored in a more systematical and technical study beyond the scope here.

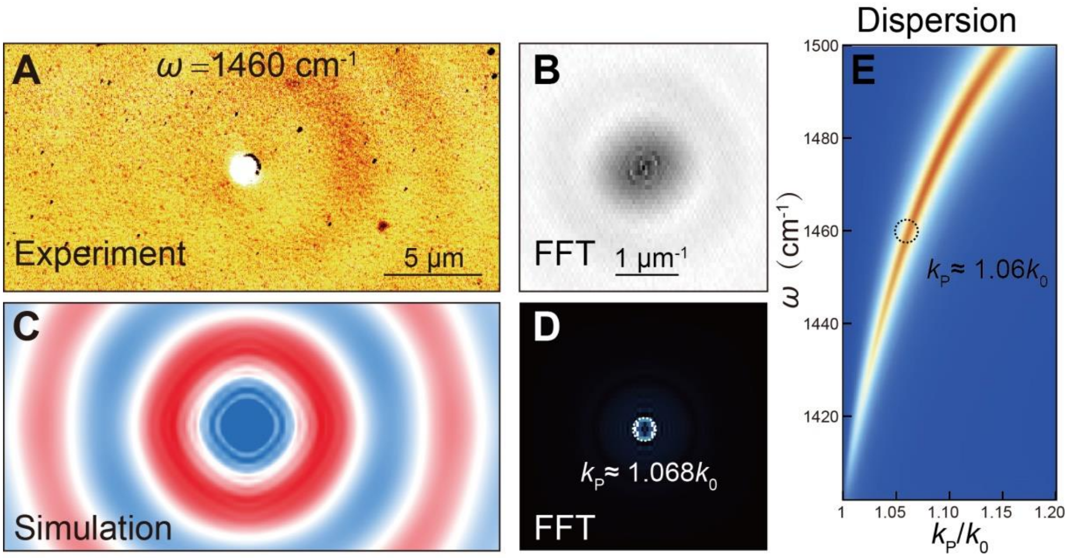

Figure S10. Analysis of experimental near-field images of disk-launched v-HP waveguide mode on calcite ($\theta = 90^o$). (**A**) Experimental near-field image of antenna-launched v-HP waveguide modes on the 50-µm-thick calcite at ω = 1460 cm^{-1}, shown in Fig. 4E of the main text. (**B**) FT of the experimental image in panel (A). (**C**) Simulated near-field image of disk-launched v-HP waveguide modes on calcite at ω = 1460 cm^{-1}. (**D**) FT of the image shown in (C). The dashed circle indicates the characteristic in-plane circular dispersion. The diameter of dashed circle indicates the momentum of polariton is about 1.068 k_0. (E) Theoretical polariton dispersion from the polaritons on a calcite substrate with $\theta = 90°$, which is calculated by using the transfer-matrix method (the calcite's layer thickness is set to be 50 µm in calculation). The black dashed circle indicates the wave vector of the polariton mode $k_p \approx 1.06\ k_0$ at ω = 1460 cm^{-1}, in excellent agreement with panel (B) and (D).

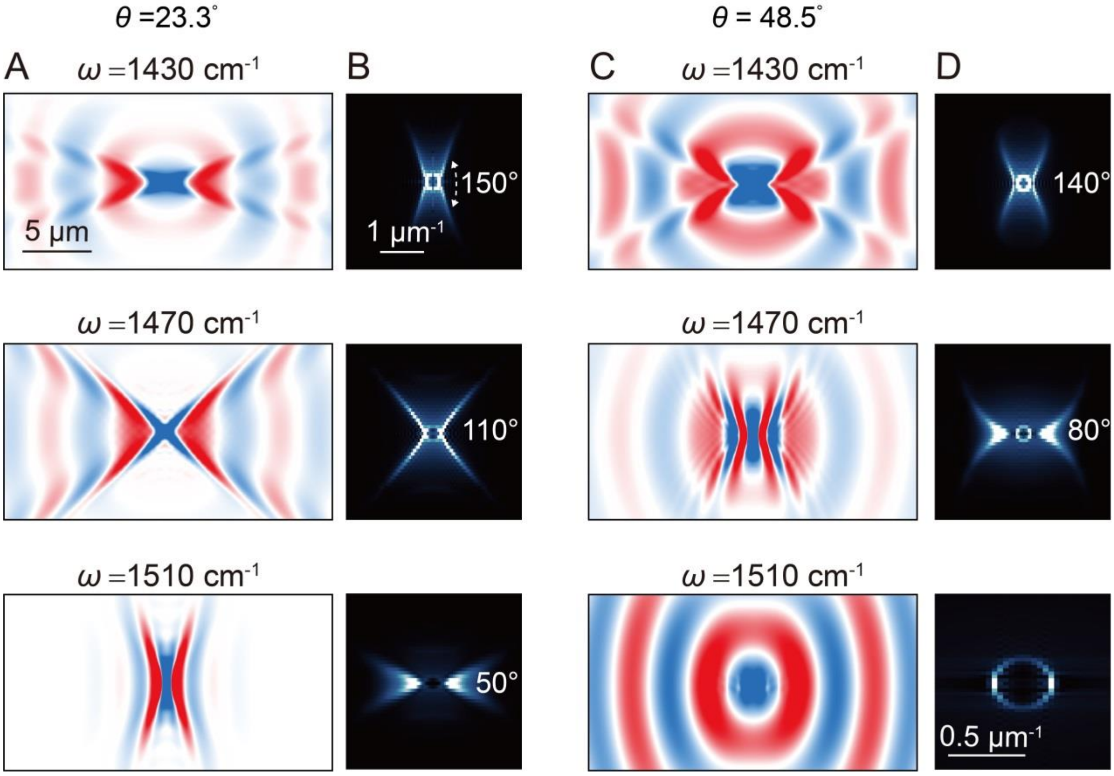

Figure S11. Frequency dependence of polariton near-field distribution on two different calcite crystals with distinct OA-orientations. (**A**) Simulated near-field distribution of polaritons on a calcite substrate with the OA-orientation angle of θ = 23.3 ° at three different frequencies. (**B**) Corresponding FT of the images shown in panel (A). (**C**) Simulated near-field distribution of polaritons on a calcite substrate with the OA-orientation angle of θ = 48.5 ° at three different frequencies. (**D**) Corresponding FT of the images shown in panel (C).

Reference

1. G. Hu, A. Krasnok, Y. Mazor, C.-W. Qiu, A. Alù, Moiré Hyperbolic Metasurfaces. *Nano Lett.* **20**, 3217-3224 (2020).
2. M. D’yakonov, New type of electromagnetic wave propagating at an interface. *Sov. Phys. JETP* **67**, 714-716 (1988).
3. K. H. Hellwege, W. Lesch, M. Plihal, G. Schaack, Zwei-Phononen-Absorptionsspektren und Dispersion der Schwingungszweige in Kristallen der Kalkspatstruktur. *Zeitschrift für Physik A Hadrons and nuclei* **232**, 61-86 (1970).
4. P. Li *et al.*, Optical Nanoimaging of Hyperbolic Surface Polaritons at the Edges of van der Waals Materials. *Nano Lett.* **17**, 228-235 (2017).
5. S. Dai *et al.*, Manipulation and Steering of Hyperbolic Surface Polaritons in Hexagonal Boron Nitride. *Adv. Mater.* **30**, 1706358 (2018).
6. S. Dai *et al.*, Tunable Phonon Polaritons in Atomically Thin van der Waals Crystals of Boron Nitride. *Science* **343**, 1125 (2014).
7. N. Ocelic, A. Huber, R. Hillenbrand, Pseudoheterodyne detection for background-free near-field spectroscopy. *Appl. Phys. Lett.* **89**, 101124 (2006).
8. A. Huber, N. Ocelic, D. Kazantsev, R. Hillenbrand, Near-field imaging of mid-infrared surface phonon polariton propagation. *Appl. Phys. Lett.* **87**, 081103 (2005).